RESEARCH PAPER

Photocatalytic Activity and Nano Structural Investigation on Co_3O_4 Nanoparticles

Mehran Riazian

Department of Engineering, Tonekabon Branch, Islamic Azad University, Tonekabon, Iran

ARTICLE INFO

Article History:
Received 28 September 2019
Accepted 14 December 2019
Published 15 February 2020

Keywords:
Photocatalytic activity
N_2 adsorption-desorption
Nanostructure
Co_3O_4

ABSTRACT

In this study, Co_3O_4 nanostructure is synthesized from the $Co(NO_3)2.6H_2O$ reactant through co-precipitation technique, and then is calcined at different calcination temperatures (CTs).The XRD peak broadening and its corresponding properties, such as lattice stress, dislocation density, X-ray density, specific area of cubic Co_3O_4 nanocrystallites, and deformation energy density are analyzed using uniform deformation model (UDM), uniform deformation stress model (UDSM), uniform deformation energy density model (UDEDM), and size-strain plot (SSP) method. Based on the XRD results, the strain of the nanocrystallites increases with the increase of CT. The lattice, structural properties, and morphology of the nanoparticles (NPs) during the CT are studied. NPs calcined at 700 °C show the most lattice strain, stress, and deformation energy, and the least X-ray density and specific area. The photocatalytic activity of Co_3O_4 (NPs) is specified by the decoloration of methylene blue (MB). Based on the results, the Co_3O_4 NPs calcined at 700 °C show the most photocatalytic activity. Furthermore, the activation energy of NPs, surface topography, pore size distribution, specific surface area, and crystallization of phases, during thermal treatment, are investigated by the BJH and BET methods.

How to cite this article
Riazian M. Photocatalytic Activity and Nano Structural Investigation on Co_3O_4 Nanoparticles. Nanochem Res, 2020; 5(1):46-58. DOI: 10.22036/ncr.2020.01.005

INTRODUCTION

Recently, Co_3O_4 nanoparticles have been widely used in various applications of medical, industry, data storage devices, catalysts, photocatalyst, gas sensors, rechargeable batteries, pigments, magnetic fluids, and optical thin films [1-3]. Co_3O_4 is a transition metal oxide and p-type semiconductor that has been attractively considered for its optical, electrical, and magnetic properties due to different states of cobalt in oxygen absorbed [4]. The physical, chemical properties and performances of Co_3O_4 nanoparticles (NPs) in mentioned applications intensively depend on the particle size, shape, geometry, dimension, and morphology [5]. Various routes and methods have been made for fabricating Co_3O_4 NPs, including pulsed laser deposition [6], chemical spray pyrolysis [7, 8], sol-gel method [9], solvo-thermal [10], reduction-oxidation route [11], cobalt salt decomposition [12], hydrothermal [13], chemical combustion [14] and mechanochemical method [15]. Most of the above-mentioned methods are complex, expensive and inconvenient to synthesize of Co_3O_4 NPs. Even though the sol-gel method seems to be a low cost processes, it has some disadvantages and limitations due to high-temperature synthesis conditions and less homogeneity. Among all the above methods, co-precipitation is accompanied by low cost, low temperature, high yields of product, versatile, and needs to fewer solvents, decrease pollutions, high controlling, and great chemical homogeneity [16,17].

Conventional oxidation methods are unable to eliminate the complex organic pollutants especially

* Corresponding Author Email: *m.riazian@toniau.ac.ir*

textile dyes. The advanced oxidation processes (AOPs) have been drastically degraded the harmful and indecomposable chemical compounds to smaller and nature-friendly compounds via highly reactive radicals $\left(.OH^-, .H^+\right)$ [18-20]. The Co_3O_4 NPs have an acceptable photocatalytic activity of dyes such as methylene blue.

This research focuses on the synthesis of Co_3O_4 NPs by co-precipitation method without using any templates, catalysts and contaminations; furthermore, it investigates the effect of CT on the strain, morphology and photocatalytic activity of Co_3O_4 NPs. The degradation rate of methylene blue in an aqueous solution contains Co_3O_4 NPs under UV. exposure which is assigned as a measure of its photocatalytic activity.

EXPERIMENTAL PROCEDURES AND DETAILS

The precursor materials and experimental conditions used for Co_3O_4 nanoparticles synthesized by the co-precipitation method are $Co(NO_3)_2.6H_2O$ (Merck ≥ 99%), ethanol (Merck ≥ 99%), deionized water, and HNO_3 (Merck ≥ 63%). The molar ratio of precursors is $Co(NO_3)_2.6H_2O$ / HNO_3/H_2O=1:4:2. First, cobalt nitrate is dissolved in deionized water and vigorously stirred with a magnetic stirrer. Afterward, HNO_3 is dropped accurately to the starting solution and adjusted at pH=4. The solution is ultrasonicated for 10 min at 45 kHz (model: Sono Swiss). A purple solution emerges, and it is stirred for about 60 h until a dark precipitate appears. Subsequently, the precipitation is dried in the oven for 12 h at 85 °C and rinsed several times thoroughly with deionized water to eliminate any pollutants and residual ions. The rinsed precipitation is dried again. The dark purple cobalt hydroxide solid is grounded in an agate mortar for 10 min to form a fine powder. Afterward, the powder is calcined at 400, 500, 600 and 700 °C with 15 C°/min heat gradient, stayed for 2 h and cooled down with the same condition.

The X-ray diffraction (XRD) is applied (GBC-MMA) using K_α(Cu) radiation λ= 0.1540 *nm*, 0.02° step size and 10 deg/min exposure speed. XRD patterns are recorded from 10-80°. The particle size and structure of the nanocrystallites are determined from transmission electron microscopy (TEM, model: Philips, CM120). Scanning electron microscopy (SEM, model: Hitachi S-4160) equipped by EDX is utilized to take images of nanoparticles. The FTIR spectrum is recorded on (model: Perkin-Elmer 783) with the sample as KBr thin tablet. The photodegradation of MB is carried out under UV. exposure (model: Philips, 254 nm, 33.6 $\mu w/cm^2$). The photocatalytic activity of Co_3O_4 nanopowders is determined by decoloration of MB and measured with UV.-Vis. spectrophotometer (model: Varian 50 scan). All experimental procedures and concentration of Co_3O_4 as a photocatalyst and MB are cited in our previous work [21,22]. The temperature of the photoreactor is fixed at 27.0 ± 0.5 °C by a small ventilator. The reaction stock solution is provided by adding 30 mg of Co_3O_4 nanopowders calcined at different CTs into 100 ml MB aqueous solution.

RESULTS AND DISCUSSION

The XRD patterns of the precipitate calcined at 400, 500, 600 and 700 °C are revealed in Fig. 1. As seen, all prominent peaks intensities of (111), (220), (311), (222), (511) and (440) could confirm to a Co_3O_4 cubic crystallite phase (Space group: Fd3m and lattice parameter, a= 8.08 $\dot{A}$). These peaks and corresponding angles (2θ) show acceptable agreement with the Joint Committee on Powder Diffraction Standards data [JCPDS-42-1467] [23]. The interplanar space values and Miller indices can be obtained from the Bragg formula (nλ=2d sin θ). The cubic lattice constant (a) and cubic cell volume of Co_3O_4 nanoparticles (V), calculated from the lattice geometry equation, Equation 1, are tabulated in Table 1, as follow:

$$\frac{1}{d^2} = \frac{h^2 + k^2 + l^2}{a^2} \quad (1)$$

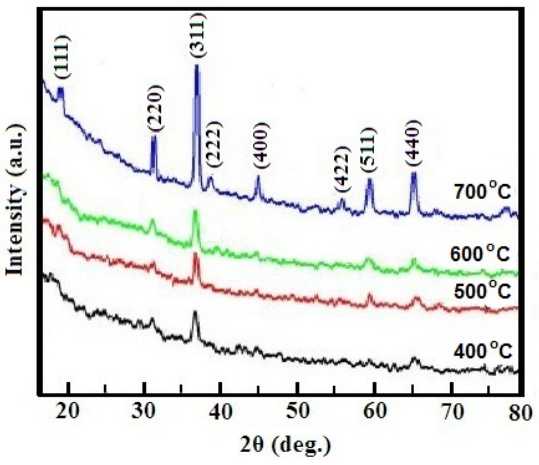

Fig. 1. XRD patterns of Co_3O_4 nanocrystallites calcined at different CTs.

$$V = a^3 \quad (2)$$

$$D_x = \frac{8M}{Na^3} \quad (3)$$

$$S_a = \frac{6}{LD_x} \quad (4)$$

where M is the molecular weight, a is the cubic lattice constant, N denotes Avogadro's constant and L is the Co_3O_4 nanocrystallite size. As seen in Table 1, the estimated values of D_x increase by increasing the CT while, the values of S_a decrease by increasing the crystallite size and CT.

The dislocation density (δ) is defined as the number of defects in the crystallite lattice that could be estimated by the experimental relationship with the crystallite size from Equation (5):

$$\delta = \frac{1}{L^2} \quad (5)$$

where L is the crystallite size. As shown in Table 1, the dislocation density of the Co_3O_4 nanocrystallites decreases by increasing the CT and nanocrystallite size.

It is worth noting that peak width broadening due to instrumental amplification causes to increase the size and lattice strain of nanocrystallites [24]. In order to eliminate the instrumental contribution (β_{inst}) of measured broadening (β_{meas}), the line broadening of standard material such as silicon is utilized. The corrected instrumental broadening associated with the diffraction peak of cubic Co_3O_4 nanoparticles is estimated by using the following equation:

$$\beta_D = [(\beta)^2_{meas} - (\beta)^2_{inst}]^{\frac{1}{2}} \quad (6)$$

There are not any extra peaks that correspond to impurities and uninvited materials. The intensity of diffraction peaks increases with increasing CT. This increase is attributed to the improvement of crystallinity quality, thermal stability and growth of boundaries. According to Fig. 1, low CT shows less peak intensity as well as a low degree of crystallization. The Co_3O_4 crystallite grain size is measured from the broadening of the peaks correspond to the Scherrer equation:

$$L = \frac{0.94\lambda}{\beta Cos\theta} \quad (7)$$

therein, L is the crystallite size (nm), β is the full width at half maximum of peaks (radians), λ is the wavelength of CuK_α (1.54 Å) and θ is the Bragg's angle corresponding to prominent and maximum intensity peak (311) at 2θ= 37.1°. As shown in Table 1, the average crystallite size increases by increasing the CT. This enlargement is due to the growth of the grain boundaries and increasing the rate of crystallite nucleation. This implies that the size distribution could be controlled by varying the CT. Table 1 presents the XRD data of the Co_3O_4 crystallite phase. The Sherrer equation considers only the instrumental corrected broadening corresponding to crystallite size without strain effect.

Williamson-Hall (W-H) method attributes the peak broadening not only to the contribution of nanocrystallite size but probably also to the strain and lattice defects. This assumption could be represented as:

$$\beta_{hkl} = \beta_D + \beta_S \quad (8)$$

$$\beta_{hkl} = \left(\frac{k\lambda}{Lcos\theta}\right) + 4\varepsilon tan\theta \quad (9)$$

$$\beta_{hkl} cos\theta = \frac{k\lambda}{L} + 4\varepsilon sin\theta \quad (10)$$

Table 1. The XRD characteristics: 2θ angle, d-space (d), the grain size of Co_3O_4 nanocrystallites at different CTs.

400 °C			500 °C			600 °C			700 °C		
2Θ	d-space(nm)	size(nm)	2Θ	d-space(nm)	size(nm)	2Θ	d-space(nm)	size(nm)	2Θ	d-space(nm)	size(nm)
18.91	0.468		18.92	0.467		18.90	0. 470		18.94	0.465	
30.89	0.285		30.88	0.286		30.87	0.289		30.88	0.287	
37.10	0.241	23.1	37.08	0.242	33.44	36.80	0.243	42.51	36.60	0.245	52.91
38.03	0.228		38.02	0.228		38.05	0.225		38.01	0.229	
44.61	0.203		44.64	0.201		44.71	0.200		44.59	0.208	
56.36	0.188		56.35	0.190		56.38	0.182		56.41	0.179	
59.46	0.153		59.45	0.153		59.44	0..155		59.42	0.158	
65.05	0.144		65.01	0.147		65.08	0.140		65.07	0.139	

where β_{hkl} denotes the total breadth of diffraction peak, β_D is the corrected instrumental broadening, β_S is the micro-strain contribution of broadening, ε is the elastic lattice strain, shape factor k is 0.94 to Scherrer's shape factor and λ= 0.1540 nm. According to the above assumption, uniform deformation method (UDM) consider the strain to be uniform in all crystallographic directions. The UDM plot is depicted with ($\beta_{hkl}Cos\theta$) in terms of the associated values of ($4Sin\theta$) for the preferred orientation peaks for different CTs (Fig. 2(a)). The values of nanocrystallite size and elastic lattice strain are calculated from the Y-intercept and slope of the fitted line.

According to uniform stress deformation Method (USDM), based on the generalized Hook's law and anisotropic nature of crystallite structure, there is a linear relationship between elastic lattice strain (ε) and lattice stress (σ) that is expressed by:

$$\sigma = \varepsilon E_{hkl} \tag{11}$$

$$\beta_{hkl}cos\theta = \frac{k\lambda}{L} + 4\frac{\sigma sin\theta}{E_{hkl}} \tag{12}$$

where E_{hkl} is the Young's modulus in the direction perpendicular to the lattice plane (hkl) associated with the mentioned prominent peaks. The validity of this method is in the range of low strain.

The Young's modulus and relationship with its elastic compliances (S_{ij}) are given by the following formula:

$$\frac{1}{E_{hkl}} = s_{11} - 2S_0\frac{(hk)^2+(lk)^2+(hl)^2}{\left(h^2+l^2+k^2\right)^2},$$

$$S_0 = S_{11-}S_{12} - \frac{S_{44}}{2} \tag{13}$$

where S_{11}, S_{12} and S_{44} are the elastic compliances of the Co_3O_4 cubic crystallite phase and their values are estimated as 4.99, -2.36 and 14.08 $(Tpa)^{-}$

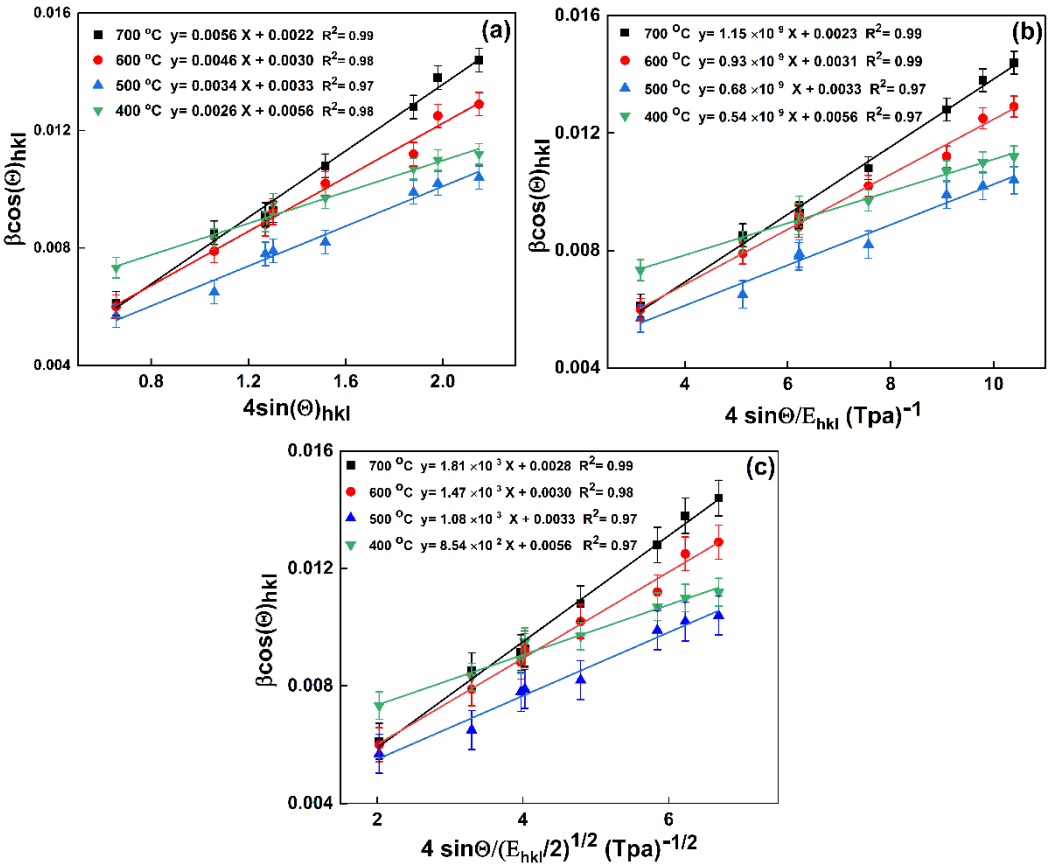

Fig. 2. The modified models of W-H analysis of the cubic crystallite phase of Co_3O_4 nanoparticles at differnet calcination temperature (a) UDM, (b) USDM, (c) UDEDM.

[1], respectively [25]. The Young's modulus (E_{hkl} is determined to be about 209.07 GPa for (111), 206.82 GPa for (220), 204.41 GPa for (311), 209.07 GPa for (222), 200.40 GPa for (400), 206.91 GPa for (422), 202.18 GPa for (511) and 206.82 GPa for (440). The average Young's modulus ($\bar{E}$) value for the Co_3O_4 cubic crystallite phase is calculated as 205.71 GPa.

As seen in Fig. 2(b), the uniform deformation stress (σ) and crystallite size could be calculated from the slope and Y-intercept of the fitted line depicted between $\frac{4sin\theta}{E_{hkl}}$ and $\beta_{hkl}cos\theta$, respectively.

Accepting the homogeneity and isotropy nature of crystallites is not correct in many cases. Furthermore, the linear dependency between stress and strain through the Young's modulus and generalized Hook low ($u = E_{hkl}\frac{\varepsilon^2}{2}$) could be considered to determine the deformation energy density (u). Therefore, the modified form of Eq. (12) is given by:

$$\beta_{hkl}cos\theta = \frac{k\lambda}{L} + 4\sin\theta\left(\frac{2u}{E_{hkl}}\right)^{\frac{1}{2}} \quad (14)$$

Fig. 2(c) indicates the plot of $\beta_{hkl}cos\theta$ versus $4\sin\theta\left(\frac{2u}{E_{hkl}}\right)^{\frac{1}{2}}$. According to the plot, u and L could be calculated from the slope and Y-intercept of the fitted line, respectively. The W-H models consider the isotropic peak broadening due to isotropic diffraction domains and micro-strain contributions. In the condition of isotropic line broadening, it is possible to acquire a beneficial assessment of size-strain parameters by regarding an average size-strain plot (SSP). According to this approach, more contribution and influence are assigned to the low-angle reflections, where the accuracy and precision are generally more than the high-angle data. This selective election reduces the scattering of data points around the linear fitted line in size-strain plot. Halder-Wanger model assumes that the profiles of the size and lattice strain are characterized by a Lorentzian and Gaussian function, respectively [26]. Accordingly, the SSP method can be written as:

$$(\beta_{hkl}d_{hkl}cos\theta)^2 = \frac{K}{L}\left(d^2{}_{hkl}\beta_{hkl}cos\theta\right) + \left(\frac{\varepsilon}{2}\right)^2 \quad (15)$$

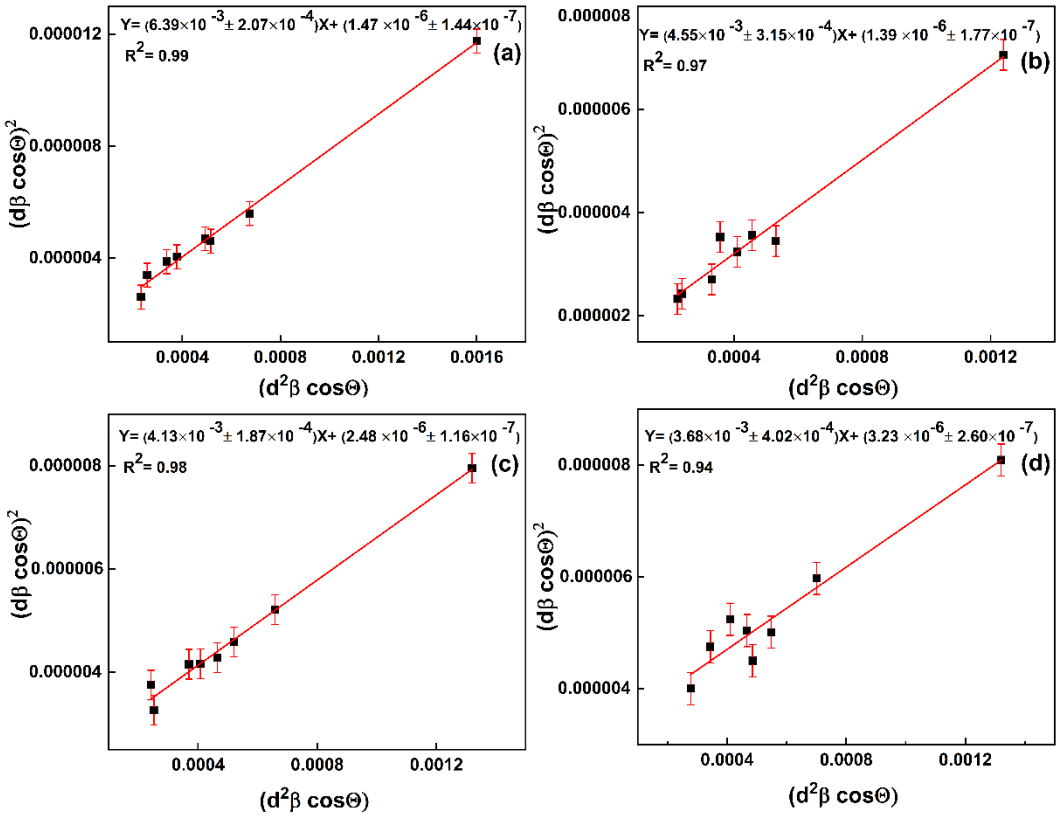

Fig. 3. Variations of versus for cubic crystallite phase of Co_3O_4 nanoparticles at (a) 400 °C, (b) 500 °C, (c) 600 °C and (d) 700 °C.

where k is a shape constant for spherical and regarded as 4/3. As indicated in Fig. 3, $(\beta_{hkl} d_{hkl} cos\theta)^2$ versus $(d^2_{hkl} \beta_{hkl} cos\theta)$ for the all intensive peaks of Co_3O_4 cubic crystallite phase is plotted. The mean value of the strain and crystallite size is determined by the y-intercept and slope of linear fitted data, respectively. The resulted data from the W-H and H-W methods are summarized in Table 2.

There is a proper linear relationship due to the existence of good crystallization at high CTs. As seen in Figs. 2 and 3, the elastic lattice strain increases with increasing the CT in all elastic deformation models. This increase is attributed to the more broadening and more grain boundaries. By increasing the CTs, it is possible to produce the required energy by the atoms to locate an appropriate position in constructing the crystallite phases [26]. The lattice strain changes d-values of diffracting planes. Nanocrystallites reveal more broadening in comparison with bulk materials due to lesser lattice planes, participating in the broadening of peaks. The broadness of peaks could occur because of lattice defects, crystal imperfection, dislocations, stacking faults, terrace vacancy and terraces. The growth process drastically affects on lattice strain. In this process, chemical bonds and ligands possess insufficient time and activation energy to diffuse to appropriate positions and sites [27-29].

The morphology of the samples that are synthesized by precipitation method is revealed with different CTs. Fig. 4(a-d) reveals morphology and remarkable aggregation of particles at low CTs. As seen, nanoparticles show less agglomeration and density with increasing CT, so that form bigger particles in the porous materials. As the CT gradually is raised from 400 °C to 700 °C, the average size of nanoparticles increases, which agrees with the XRD results. The SEM images show that the particles are somewhat spherical in shape at low CTs. The EDX pattern reveals the present chemical composition as well as the purity of Co_3O_4 nanoparticles (Fig. 5).

The total energy of Co_3O_4 nanoparticle formation could be derived by using the Scott [30] equation:

$$L = Cexp\left(\frac{-E}{RT}\right) \tag{16}$$

where L is the average nanocrystallite size, E is the activation energy, R is the ideal gas constant,

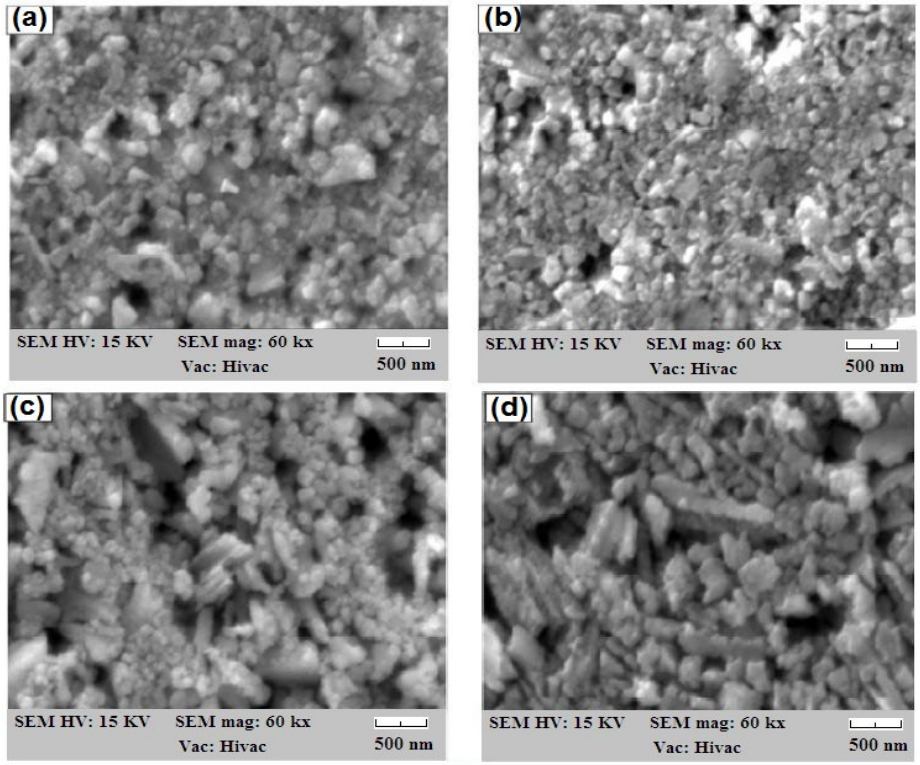

Fig. 4. The SEM images of Co_3O_4 nanoparticles calcind at: (a) 400 °C, (b) 500 °C, (c) 600 °C and (d) 700 °C.

Table 2. Structure and geometric parameters of cubic crystallite phase of Co_3O_4 nanoparticles at different CTs.

Calcination Temperate °C	UDM			USDM				UDEDM				SSP method				Lattice parameter and unite cell volume	D_x $\frac{g}{cm^3}$	S_a $\frac{cm^2}{g} \times 10^5$
	D (nm)	$\frac{\delta}{lines/m^2}$	$\varepsilon \times 10^{-3}$	D (nm)	$\frac{\delta}{lines/m^2}$	$\varepsilon \times 10^{-3}$	σ MPa	D (nm)	$\frac{\delta}{lines/m^2}$	$\varepsilon \times 10^{-3}$	σ MPa	u $(\frac{KJ}{m^3})$	D (nm)	$\frac{\delta}{lines/m^2}$	$\varepsilon \times 10^{-3}$	σ MPa	u $(\frac{KJ}{m^3})$			
400	24.75	16.32	2.68	24.45	16.72	2.63	543	24.53	16.61	2.66	548	727	21.69	21.25	2.433	500	608	a = 0.799 nm V = 0.510 nm^3	6.27	4.14
500	41.88	2.38	3.39	41.14	5.90	3.34	688	41.51	5.80	3.36	693	1164	30.46	10.77	2.35	484	571	a = 0.802 nm V = 0.515 nm^3	6.20	2.89
600	45.60	4.80	4.60	44.72	5.00	4.55	937	45.16	4.90	4.57	942	2160	33.55	8.88	3.14	647	1019	a = 0.805 nm V = 0.521 nm^3	6.13	2.30
700	61.89	2.61	5.66	59.50	2.82	5.59	1150	60.81	2.70	5.64	1160	3270	37.67	7.04	3.59	739	1328	a = 0.812 nm V = 0.535 nm^3	5.97	1.89

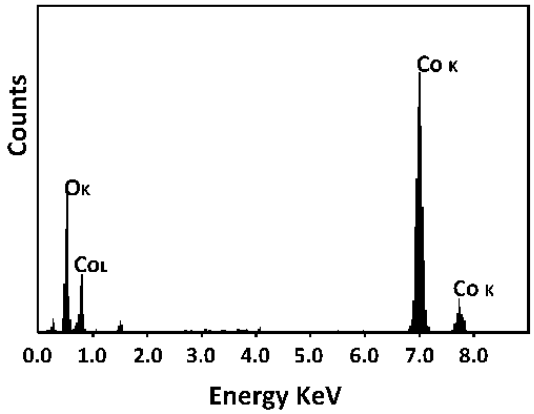

Fig. 5. EDX pattern of the Co_3O_4 nanoparticles calcined at 700°C.

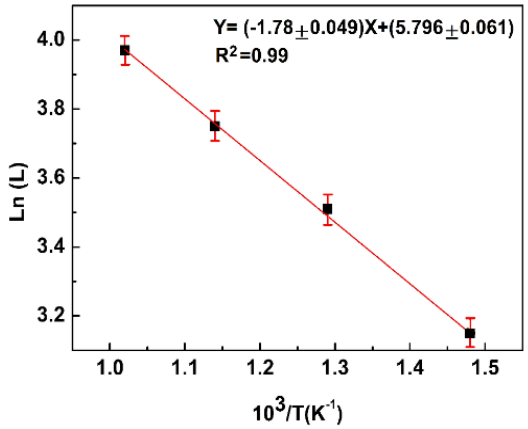

Fig. 6. CT dependence to Ln(L) for Co_3O_4 nanoparticles.

C is the constant of relation and T is the absolute temperature correspond to CTs.

The variation of *Ln(L)* versus *1/T* is plotted and fitted as a straight line (Fig. 6). It is supposed that Scott equation applied in the homogenous and unified growth of grains which explains the growth rate of crystalline grain from amorphous shape during thermal treatment. The activation energy of Co_3O_4 nanocrystallites during calcination is calculated to be 14.79 *KJ/mol*.

In order to study the chemical bonds in Co_3O_4 nanoparticles, the FT-IR spectra are carried out in the range of IR (400-4000 cm^{-1}). As shown in Fig. 7, the spectrum of the calcined Co_3O_4 nanoparticles reveals a broad absorption band in the range of 1650 and 3400-3600 cm^{-1}, which is attributed to the asymmetrical and symmetrical

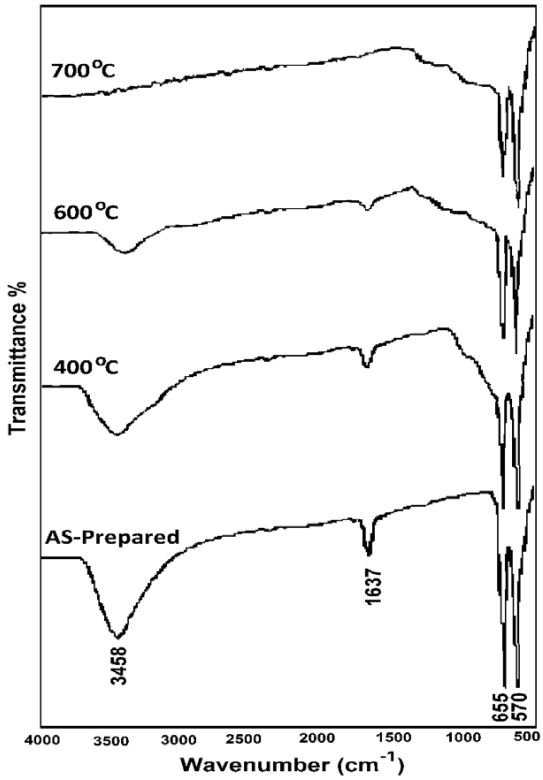

Fig. 7. FT-IR spectra of Co_3O_4 nanoparticles calcined at different temperatures.

OH bonds from co-ordinated or entrapped water. The intensity of this band decreases and evades as the CTs increases. As seen in Fig. 7, the vibration of Co^{+3} ions in octahedral holes appears at 570 cm^{-1}, and the stretching vibration in the Co^{+2} ions in the tetrahedral holes reveals at 655 cm^{-1}. These bands predicate the presence of FCC (face-centered cubic) nanocrystalline structure of Co_3O_4 nanoparticles [1,5,31].

Fig. 8 shows the TEM images of structure and morphology of Co_3O_4 nanoparticles calcined at different CTs. This figure reveals that by increasing the CTs, the growth and aggregation of nanoparticles will be augmented. The average size of nanoparticles are 40, 57, 70 and 82 nm for samples calcined at 400, 500, 600 and 700 °C, respectively. This growth is in an acceptable agreement with the XRD and SEM analyses. The samples calcined at low temperatures are partially congested, agglomerated and reveal spherical shape. By increasing the CTs, the boundaries and surface of adjacent particles interpenetrate, causing to enlarge the diameter and the size of nanoparticles, while they are partially

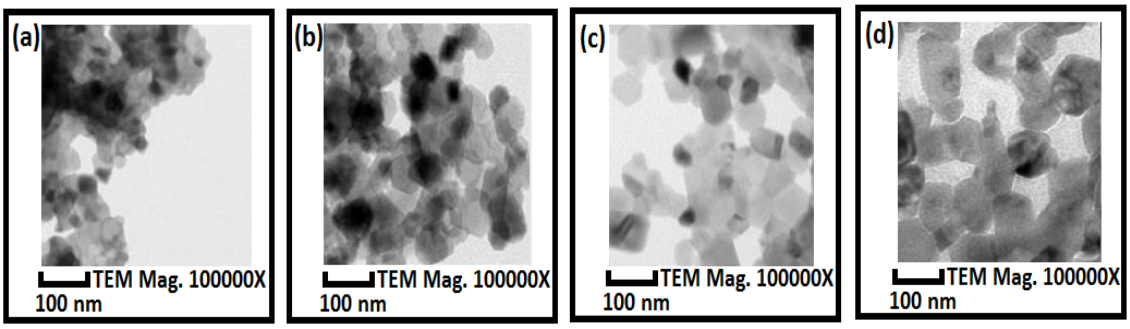

Fig. 8. TEM images of Co_3O_4 nanoparticles calcined a: (a) 400 °C, (b) 500 °C, (c) 600 °C and (d) 700 °C

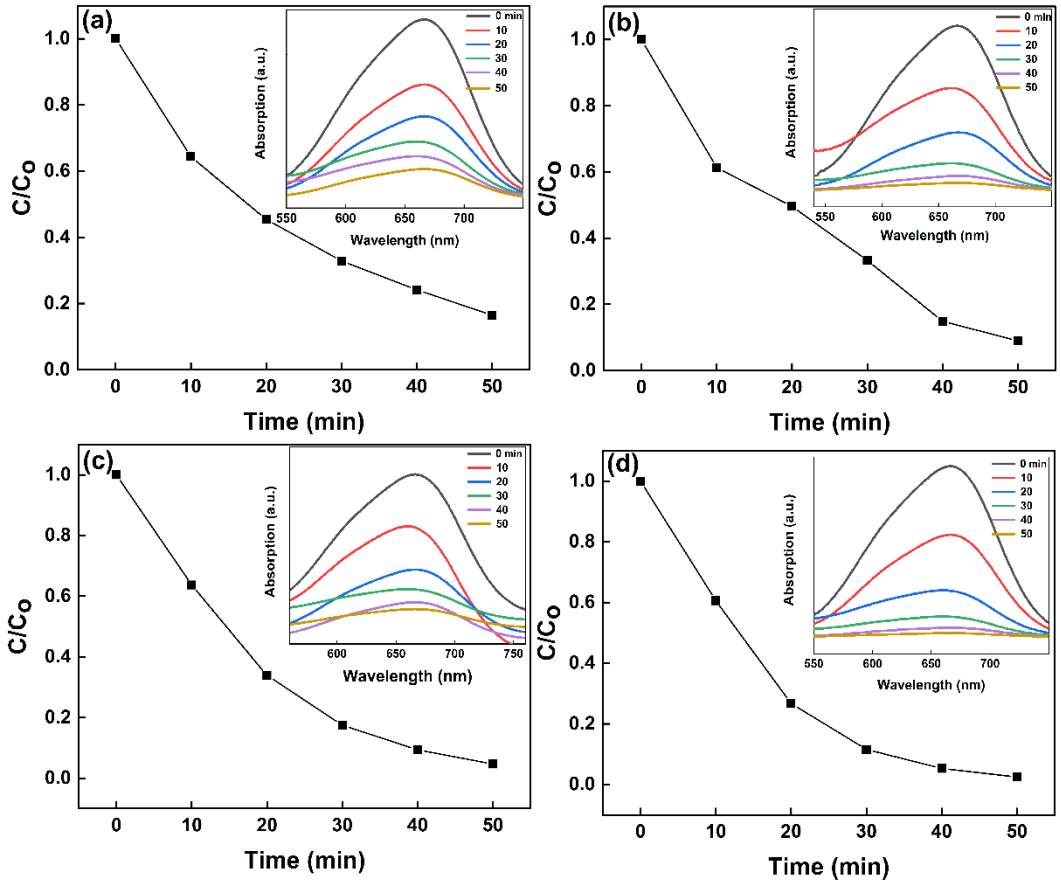

Fig. 9. Exposure Time dependence of relative concentration (C/C_0) for the Co_3O4 nanoparticles with different CTs, (a) 400 °C, (b) 500 °C, (c) 600 °C, (d) 700 °C. [Inset: absorbance peak at 660 nm and UV-visible absorbance spectra per irradiation time].

granular, uniform and cubic [32,33].

The photocatalytic activity of the photocatalyst solution is determined by the UV.-Vis. spectrophotometer at 666 nm as revealed in the inset graph of Fig. 9. Fig. 9 indicates the time-dependent absorption spectra of MB located at ($\lambda_{max} = 666 nm$). The intensity of absorption plots gradually decreases with increasing the irradiation time because of the dye decoloration. This plot shows the dependence of C/C_0 versus the time irradiation 0 to 50 minutes and illustrates the photodegradation percentage after 50 min that are about 80%, 89%, 93%, 96% for

samples were calcined at 400 °C, 500 °C, 600 °C and 700 °C, respectively.

The degradation rate of the aqueous solution of MB by Co_3O_4 NPs under UV irradiation is calculated by the equations mentioned below:

$$\text{Photodegradation Rate \%} = \text{Ln}\left[\frac{C_0 - C}{C}\right] \times 100 \quad (17)$$

$$\text{Ln}\left(\frac{C_0}{C}\right) = kt \quad (18)$$

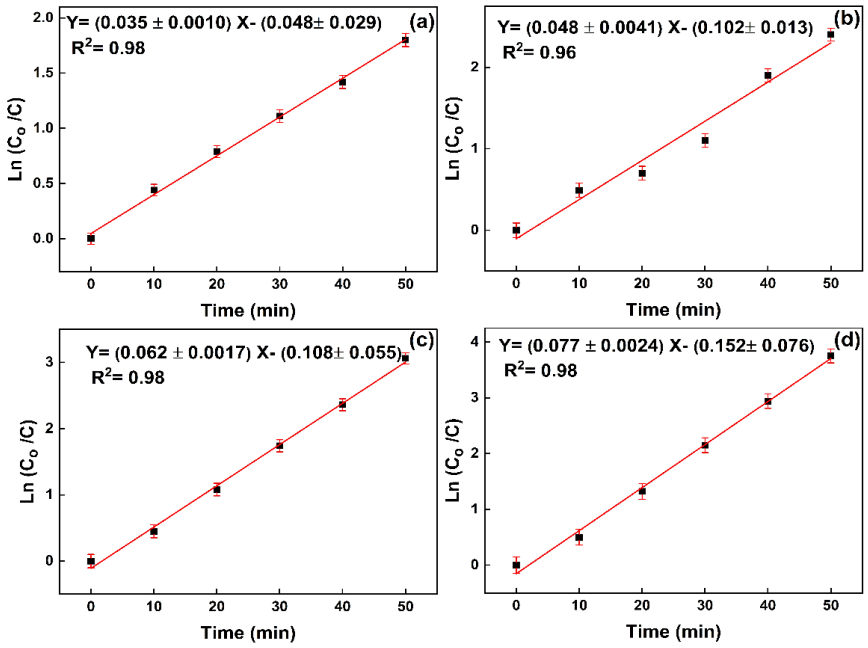

Fig. 10. Correlation between exposure time and Ln(C_0/C) for the Co_3O4 nanoparticles at different CTs, (a) 400 °C, (b) 500 °C, (c) 600 °C, (d) 700 °C.

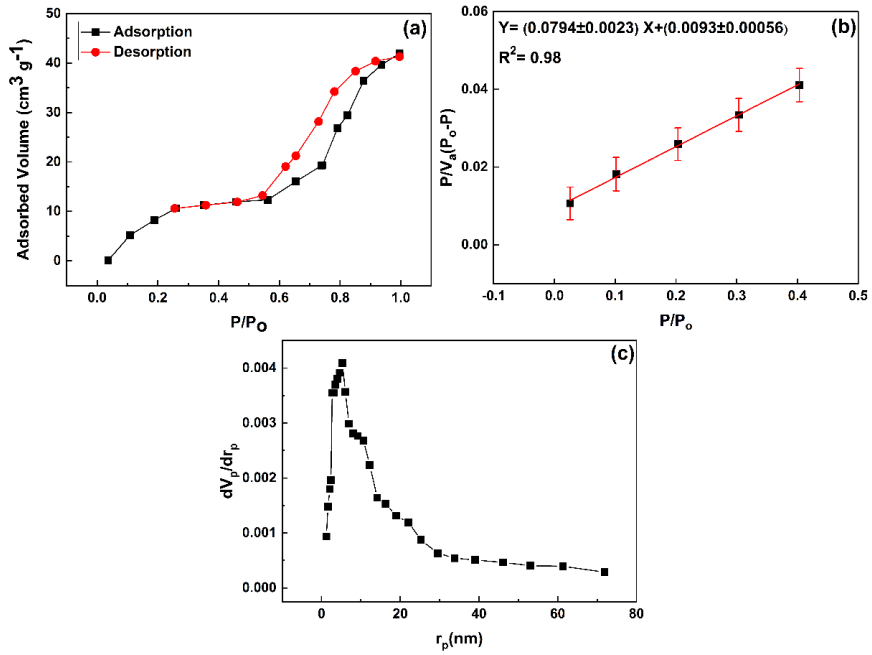

Fig. 11. (a) Isotherm adsorption-desorption plot, (b) BET plot, (c) BJH plot of Co_3O_4 nanoparticles calcined at 700 °C.

Table 3. Photodegradation rate (photocatalytic activity) of Co_3O4 nanoparticles.

Calcination Temperature °C	$k(\frac{1}{min})$	Correlation coefficient (R^2)
400	0.033	0.98
500	0.044	0.96
600	0.065	0.98
700	0.077	0.98

Table 4. N_2 physisorption data of Co_3O_4 nanoparticles calcined at 700 °C.

Total pore volume ($\frac{m^3}{g}$)	S_{BET} ($\frac{m^2}{g}$)	Mean pore diameter (nm)	$r_{p,peak}$ (nm)
0.168	58.05	11.57	5.68

The comparative concentration of MB in the logarithmic scale $Ln\left(\frac{C_0}{C}\right)$ is plotted against UV.-Vis. exposure time according to samples calcined at different CTs (Fig. 11). The slope of logarithmic plots is the rate constant of photodegradation [34]. The Photocatalytic measurements in Table 3 reveal the relevant kinetic variables, such as correlation coefficient (R^2) and the degradation rate constant (k). All reactions reveal a linear relation. As seen in Fig. 11, the rate constant, k is estimated depending on the presence of Co_3O_4 and CTs. By increasing the CTs and increasing the porosity of samples, the rate constant (k) increases, since more crystallinity of Co_3O_4 crystalline phase has an outstanding effect on the degradation of the organic complex compounds. Furthermore, the enhancement in photocatalytic efficiency has been imputed to improved thermal stability, the surface properties, surface porosity and ultimate results to generate the instant splitting of photo-induced electrons and holes and prolonging the recombination process of conduction and valence band carriers.

Fig. 11 shows the N_2 physisorption isotherm, Brunaur-Emmett-Teller (BET) and Barret-Joyner-Halenda (BJH) pore size distribution for the Co_3O_4 nanoparticles that were calcined at 700 °C. According to the adsorption-desorption (ads-des) isotherm, the Co_3O_4 nanoparticles show the IV type characteristic portends that they are microporous join with mesoporous structure. The BET specific surface area (S_{BET}), total pore volume, mean pore diameter, and pore diameter at peak of the BJH curve ($r_{p,peak}$) are derived and shown in Table 4. $r_{p,peak}$ shows the peak of the size in pore size distribution. The ads-des curves show the hysteresis loop that indicates the formation of cylindrical pores and capillary condensation in meso and micropores. The first knee indicates the approximate position of monolayer and the second knee indicates the formation of the multilayer.

CONCLUSION

The Co_3O_4 NPs were synthesized by the co-precipitation method. The nanostructure and photocatalytic performance of the prepared Co_3O_4 NPs such as the size, strain and photocatalytic activity were investigated. The CTs affected the nanostructural and optical properties. The XRD, SEM and TEM analysis revealed that average sizes of nanocrystallites increase by raising the CTs. The EDX pattern showed the presence of chemical elements as well as the purity of the Co_3O_4 nanoparticles. The XRD analysis indicated a low degree of crystallinity for samples calcined at low temperatures. The line broadening of the Co_3O_4 cubic crystallite phase related to the crystallite size and lattice strain were investigated by the W-H and H-W methods with a different assumption about the isotropic and homogeneity nature of the crystallite. Accordingly, the crystallite size, lattice strain, stress, and uniform deformation energy of the Co_3O_4 cubic crystallite phase were determined. Based on the results, the crystallite size, lattice strain, stress, and deformation energy increased as CT increased. By increasing the CT, the X-ray density and specific area of Co_3O_4 cubic crystallite phase decreased. The SEM images of the NPs showed sphere-like particles and more

congestion compared to the samples calcined at higher temperatures. The activation energy of Co_3O_4 was estimated to be 14.79 *KJ/mol*. The experimental results showed that decomposition of methylene blue under UV. irradiation had a higher photocatalytic activity by increasing the CT. The ads-des curves predicted the formation of cylindrical pores and capillary condensation in meso and micropores. The first and second knees of the ads-des plot indicated the approximate position of monolayer and the formation of multilayer, respectively. Therefore, Co_3O_4 nanoparticles could be a promising candidate to act as a gas absorbent in gas sensors. Based on the results presented, Co_3O_4 N Ps show a higher photocatalytic activity, less lattice strain and more thermal durability with increasing the CTs.

ACKNOWLEDGMENT

The author appreciates Islamic Azad University, Tonekabon Branch for its financial support throughout this research project.

CONFLICT OF INTEREST

The authors confirm that this article content has no conflict of interest.

REFERENCES

1. Zacho SL, Gajdek D, Mielby J, Kegnæs S. Synthesis of Nano-engineered Catalysts Consisting of Co3O4 Nanoparticles Confined in Porous SiO2. Topics in Catalysis. 2019;62(7-11):621-7.
2. Fort A, Panzardi E, Vignoli V, Hjiri M, Aida M, Mugnaini M, et al. Co3O4/Al-ZnO Nano-composites: Gas Sensing Properties. Sensors. 2019;19(4):760.
3. Chekuri RD, Tirukkovalluri SR. Synthesis of cobalt doped titania nano material assisted by gemini surfactant: Characterization and application in degradation of Acid Red under visible light irradiation. South African Journal of Chemical Engineering. 2017;24:183-95.
[4] Vennela A, Mangalaraj D, Muthukumarasamy N, Agilan S, Hemalatha K. Structural and optical properties of Co_3O_4 nanoparticles prepared by sol-gel technique for photocatalytic application. Int J Electrochem Sci. 2019;14:3535-52.
5. Brito SLM, Gouvêa D, Ganzella R. Estudo da adsorção de dispersante à base de poliacrilato em um sistema varistor comercial: caracterização físico-química. Cerâmica. 2005;51(317):30-6.
6. Warang T, Patel N, Santini A, Bazzanella N, Kale A, Miotello A. Pulsed laser deposition of Co3O4 nanoparticles assembled coating: Role of substrate temperature to tailor disordered to crystalline phase and related photocatalytic activity in degradation of methylene blue. Applied Catalysis A: General. 2012;423-424:21-7.
7. Louardi A, Rmili A, Ouachtari F, Bouaoud A, Elidrissi B, Erguig H. Characterization of cobalt oxide thin films prepared by a facile spray pyrolysis technique using perfume atomizer. Journal of Alloys and Compounds. 2011;509(37):9183-9.
8. Aboud AA, Abdel-Hakima S, Ali M, Afify H, Revaprasadu N. Characterization of nano-crystalline Co-La mixed oxide thin films prepared by the spray pyrolysis technique. Results in Physics. 2019;12:1513-9.
[9] Farahmandjou M. Fabrication and characterization of nanoporous Co oxide (Co_3O_4) prepared by simple sol-gel synthesis. Physical Chemistry Research. 2016;4(2):153-60.
10. Sun L, Li H, Ren L, Hu C. Synthesis of Co3O4 nanostructures using a solvothermal approach. Solid State Sciences. 2009;11(1):108-12.
11. Ozkaya T, Baykal A, Koseoğlu Y, Kavas H. Synthesis of Co3O4 nanoparticles by oxidation-reduction method and its magnetic characterization. Open Chemistry. 2009;7(3):410-4.
12. Farhadi S, Javanmard M, Nadri G. Characterization of Cobalt Oxide Nanoparticles Prepared by the Thermal Decomposition. Acta Chimica Slovenica. 2016:335-43.
13. Kang M, Zhou H. Facile Synthesis and Structural Characterization of Co_3O_4 Nanocubes. AIMS Materials Science. 2015;2(1):16-27.
14. Merino MCG, Rapp MEFd, Pinto M, Etchechoury ME, Lassa MS, Martínez JMM, et al. Combustion Synthesis of Ultrafine Powders of Co3O4 for Selective Surfaces of Solar Collectors. Procedia Materials Science. 2015;9:230-8.
15. García-Pacheco G, Cabañas-Moreno JG, Yee-Madeira H, Cruz-Gandarilla F. Co3O4nanoparticles produced by mechanochemical reactions. Nanotechnology. 2006;17(10):2528-35.
16. Prabaharan DDM, Sadaiyandi K, Mahendran M, Sagadevan S. Precipitation method and characterization of cobalt oxide nanoparticles. Applied Physics A. 2017;123(4).
[17] Sharifi SL, Shakur HR, Mirzaei A, Hosseini MH. Characterization of Cobalt Oxide Co_3O_4 Nanoparticles Prepared by Various Methods: Effect of Calcination Temperatures on Size, Dimension and Catalytic Decomposition of Hydrogen Peroxide. International Journal of Nanoscience and Nanotechnology. 2013;9(1):51-8.
18. Balgude SD, Sethi YA, Kale BB, Amalnerkar DP, Adhyapak Parag V. ZnO decorated Sn3O4 nanosheet nano-heterostructure: a stable photocatalyst for water splitting and dye degradation under natural sunlight. RSC Advances. 2019;9(18):10289-96.
[19] Abbasi A, Ahmadi Golsefidi M, Mohammad Beigi M, Sadri N, Abroudi M. Facile Fabrication of Co3O4 Nanostructures as an Effective Photocatalyst for Degradation and Removal of Organic Contaminants. Journal of Nanostructures. 2018;8(1):89-96.
[20] Poorarjmand S, Kargar Razi M, Mahjoob AR, Khosravi M. Photocatalytic degradation of Congo Red dye by using nano ZnO and Ni-Co-ZnO nanocomposites. Journal of Nanoanalysis. 2018;5(2):99-105.
21. Shabanpour S, Riazian M. Synthesis and photocatalytic properties of nano iron oxide. Micro & Nano Letters. 2018;13(3):378-82.
22. Riazian M, Yousefpoor M. Photocatalytic activity, nanostructure and optical properties of 3D ZnS urchin-like via hydrothermal method. International Journal of Smart and Nano Materials. 2020;11(1):47-64.
23. Mote VD, Purushotham Y, Dole BN. Structural,

morphological and optical properties of Mn doped ZnS nanocrystals. Cerâmica. 2013;59(352):614-9.
24. Al-Tabbakh AA, Karatepe N, Al-Zubaidi AB, Benchaabane A, Mahmood NB. Crystallite size and lattice strain of lithiated spinel material for rechargeable battery by X-ray diffraction peak-broadening analysis. International Journal of Energy Research. 2019;43(5):1903-11.
[25] Tromans D. Elastic anisotropy of HCP metal crystals and polycrystals. Int J Res Rev Appl Sci. 2011;6(4):462-83.
26. Motevalizadeh L, Heidary Z, Abrishami ME. Facile template-free hydrothermal synthesis and microstrain measurement of ZnO nanorods. Bulletin of Materials Science. 2014;37(3):397-405.
27. Riazian M. NANOSTRUCTURAL CHARACTERIZATION AND LATTICE STRAIN OF TiO2-Al2O3-SiO2 COATING ON GLASS AND SI (100) SUBSTRATES. Journal of the Chilean Chemical Society. 2016;61(2):2870-7.
[28] Riazian M. Synthesis of pure and aluminum oxide doped TiO_2 nanorods and study of lattice strain and activation energy of crystalline phases. Indian Journal of Chemistry. 2014;53A:1377-83.
29. Riazian M, Rad SD, Azinabadi RR. Fabrication of pure and Ag-doped TiO2 nanorods and study of the lattice strain and the activation energy of the crystalline phases. Journal of the Korean Physical Society. 2013;62(3):459-68.
[30] G. SM. Amorphous Metallic Alloys London: Butterworth.151.
31. Farhadi S, Safabakhsh J, Zaringhadam P. Synthesis, characterization, and investigation of optical and magnetic properties of cobalt oxide (Co3O4) nanoparticles. Journal of Nanostructure in Chemistry. 2013;3(1).
32. Naseri MG, Saion EB, Hashim M, Shaari AH, Ahangar HA. Synthesis and characterization of zinc ferrite nanoparticles by a thermal treatment method. Solid State Communications. 2011;151(14-15):1031-5.
33. Naseri M. Optical and magnetic properties of monophasic cadmium ferrite (CdFe2O4) nanostructure prepared by thermal treatment method. Journal of Magnetism and Magnetic Materials. 2015;392:107-13.
[34] Parhizkar J, Habibi MH. Investigation and Comparison of Cobalt ferrite composite nanoparticles with individual Iron oxide and Cobalt oxide nanoparticles in azo dyes removal. Journal of Water and Environmental Nanotechnology. 2019;4(1):17-30.